CHEMISTRY OF MATERIALS

Article

pubs.acs.org/cm

Structural Characterization and Redox Catalytic Properties of Cerium(IV) Pyrochlore Oxides

Helen Y. Playford,[†] Deena R. Modeshia,[†] Emma R. Barney,[‡] Alex C. Hannon,[‡] Christopher S. Wright,[§] Janet M. Fisher,[⊥] Alvaro Amieiro-Fonseca,[⊥] David Thompsett,[⊥] Luke A. O'Dell,[∥] Gregory J. Rees,[∥] Mark E. Smith,[∥] John V. Hanna,[∥] and Richard I. Walton*[,†]

[†]Department of Chemistry and [∥]Department of Physics, University of Warwick, Coventry, CV4 7AL, U.K.

[‡]ISIS Facility, Rutherford Appleton Laboratory, Harwell Science and Innovation Campus, Didcot, OX11 0QX, U.K.

[§]Sigma-Aldrich Company Ltd, Fancy Road, Poole, Dorset, BH12 4QH, U.K.

[⊥]Johnson Matthey Technology Centre, Sonning Common, Reading, RG4 9NH, U.K.

Supporting Information

ABSTRACT: Ce(IV) pyrochlore oxides have been prepared by hydrothermal synthesis, and the parent material, a sodium cerium titanate, has been studied using total neutron scattering. While analysis of Bragg diffraction is consistent with an average cubic pyroclore structure, the profile is broadened because of the crystal size of <10 nm. Analysis of the pair distribution function (PDF) produced by Fourier transformation of the total scattering yields a structural model consistent with formulation of the parent material as $(Na_{0.33}Ce_{0.53}Ti_{0.14})_2Ti_2O_7$. This contains a proportion of A-site titanium, consistent with the measured bulk density of the material. The PDF also contains evidence that the short-range order of the pyrochlore structure is disordered, with oxide anions displaced from the positions of the ideal $Fd\bar{3}m$ pyrochlore structure to give local symmetry $F\bar{4}3m$. These observations are supported by static (broadline) solid state ^{49}Ti NMR measurements on a ^{49}Ti isotopically enriched sample, which showed a dominant, narrow resonance at an apparent shift of δ − 912 ppm and a second minor resonance consistent with A-site titanium. Sn(IV) doping of the pyrochlore phase is possible by one-step hydrothermal synthesis: this gives a series of materials with a maximum tin content of Sn:Ti = 0.4:0.6, for which ^{119}Sn solid-state NMR confirms the presence of octahedral, B-site Sn(IV), and powder X-ray diffraction shows an associated expansion of the pyrochlore lattice. Temperature programmed reduction/oxidation studies of the materials reveal that after an activation cycle the parent pyrochlore shows a reversible low temperature reduction at <200 °C, more facile than ceria itself. The Sn-doped analogues also show a low temperature reduction, but on continued heating collapse irreversibly to yield a mixture of products that includes SnO. The parent pyrochlore has been tested as a support for gold in the water gas shift reaction and shows a lower temperature conversion of H_2O and CO to H_2 and CO_2 than a ceria sample of similar surface area.

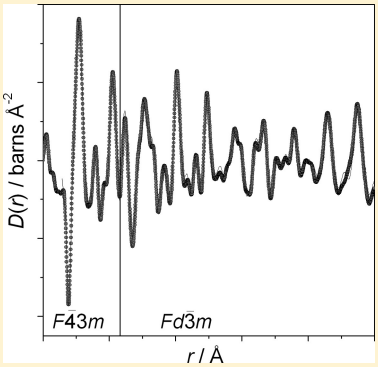

KEYWORDS: *ceria, hydrothermal, water-gas shift, total scattering, neutron diffraction*

INTRODUCTION

Cerium dioxide is well-known for its considerable uses in heterogeneous catalysis where it provides a redox-active material that makes use of the reversible reduction and reoxidation between Ce(IV) and Ce(III) in the solid-state at moderate temperatures of a few hundred degrees centigrade.[1] This activity depends on oxide-ion migration in the solid state and gives the material important uses as a catalyst support, especially for precious metals, where it is well-known for its use in three-way automotive catalytic convertors for the removal of noxious gases from combustion of fossil fuels. Here, ceria primarily acts as an oxygen level buffer to maintain optimal air/fuel ratio for conversion of CO, NO_x, and uncombusted hydrocarbons.[2] An ongoing challenge in this situation is to produce ceria-based catalysts that are active at the lower temperatures associated with the start-up of combustion engines, where pollutant concentrations are high.[3]

Another contemporary use of ceria is as a catalyst support in the water gas shift (WGS) reaction, the conversion of carbon monoxide and water to carbon dioxide and hydrogen.[4] This is important for the efficient generation and purification of hydrogen for new and future energy sources.[5,6] In particular, in proton-exchange membrane fuel cells, low temperature WGS catalysts are useful for the removal of CO from the fuel feed produced by steam reforming of natural gas, to prevent poisoning of the fuel cell electrode.[5,7] WGS catalysis is additionally believed to have an important role in the operation

Received: September 28, 2011
Revised: November 9, 2011
Published: November 9, 2011

of automotive three way catalysts.[8] Industrial WGS catalysts are based upon a combination of CuO, Al_2O_3, and ZnO, but these materials are highly reactive towards air, and also copper-based catalysts are not robust enough to maintain activity in the start-up/shut-down cycles associated with small-scale applications such as fuel processor units. Hence, novel materials must be sought which can be easily handled and possess the recyclability required for small-scale hydrogen purification.[9] A particular challenge is the preparation of new and improved catalyst materials that have high activity at low temperatures (ideally less than 650 K), since the forward WGS reaction is exothermic, and hence lower temperatures must be used to optimize productivity.[10] Gold or platinum supported on ceria is one system that has been recently investigated for WGS[11] and it has recently been shown that a very strong Au-ceria interaction, on an atomic scale, is responsible for the high activities of the gold-loaded materials,[12] although the precise mechanism of activity of these materials remains the topic of some debate.[13]

In tuning the properties of ceria, a common strategy is doping, either with isovalent cations, such as Zr^{4+} [14] and Sn^{4+},[15] that may induce lattice distortion and hence aid oxide-ion migration in the solid-state, or by aliovalent cations, such as Y^{3+}, Gd^{3+}, Sm^{3+}, Bi^{3+}, and Sr^{2+} whose lower charge introduces compensating oxide ion vacancies to further enhance oxide-ion migration.[16] In addition, transition-metal cations such as Ti^{4+},[17] Cu^{2+},[18] Fe^{3+},[19] and Pd^{2+} [20] have also been introduced as dopants into CeO_2, and these metals themselves may show additional redox activity. Although doping has proved to be successful means of tuning redox activity of ceria, in the continued development of highly active materials with low temperature activity it is important to consider novel cerium(IV)-containing materials. For complex materials to be active as catalysts it is desirable to use synthetic strategies that also offer some control of crystal form to ensure that finely divided particles are available, and hence low-temperature routes such as solvothermal synthesis are desirable.[21] With this in mind, we have investigated the synthesis of cerium(IV) titanate oxides and previously reported a novel pyrochlore material, with assumed composition $(Na_{0.33}Ce_{0.67})_2Ti_2O_7$ from powder X-ray diffraction analysis, by a one-step hydrothermal route from metal salts in the presence of an oxidizing agent.[22] Our preliminary studies of its redox properties using temperature programmed reduction (TPR) and XAFS showed the material to exhibit superior properties over ceria itself, which we attributed to enhanced oxide-ion mobility in the pyrochlore structure, a structure related to the fluorite lattice but with intrinsic oxide-ion vacancies.[22,23] In this paper we present the results of a full structural characterization of the material, an investigation of doping, new results from TPR and temperature programmed oxidation (TPO) studies, and the results from a study of the activity of the material as a support for gold in WGS catalysis.

EXPERIMENTAL SECTION

Sample Preparation. In a typical synthesis of the sodium cerium titanate pyrochlore, 0.37 g of $CeCl_3.7H_2O$ (Sigma-Aldrich), 0.26 g of TiF_3 (Sigma-Aldrich), and 0.375 g of $NaBrO_3$ (Sigma-Aldrich) were stirred in a ~20 mL Teflon container with 4 mL of sodium hydroxide solution (10 M) for 30 min and made up to a total volume of 8 mL with water before sealing in a steel autoclave and placing in a preheated fan oven for 5 h at 240 °C. The reaction yields a pale yellow powder, which was recovered by suction filtration, washed thoroughly with hot water, and dried at various temperatures (see below). To minimize inhomogeniety in the sample the solid precursors were ground together before addition of the sodium hydroxide solution. Tin-doped analogues of the parent pyrochlore material were prepared by replacement of a proportion of the TiF_3 precursor by solid $Sn(OCH_2CH_3)_4$. A ^{49}Ti labeled sample of the sodium cerium titanate pyrochlore phase was prepared for solid-state NMR studies in a similar manner but using $^{49}TiO_2$ as the titanium source (used as purchased from Trace Science Isotopes with a quoted elemental abundance of ^{49}Ti of 92+ %). TiO_2 is a less reactive precursor than TiF_3, and the sample was found to be contaminated with a small amount of (presumably unreacted) rutile TiO_2 and some CeO_2, but the major phase was the same pyrochlore as when TiF_3 was used for synthesis.

X-ray Diffraction (XRD). Powder XRD data were collected using either a Siemens D5000 diffractometer, or a Bruker D8 Advance X-ray diffractometer equipped with a VÅNTEC-1 solid-state detector, both operating with Cu Kα radiation. For measurements above room temperature the latter was fitted with an Anton-Parr XRK900 chemical reaction chamber to allow measurements to be made as a function of temperature and gas environment. Samples were heated in air and patterns recorded at 50 °C intervals after holding for 6 h to achieve equilibration.

Transmission Electron Microscopy (TEM). TEM was performed using a JEOL 2000 FX Transmission Electron Microscope fitted with an EDAX Genesis analytical system. The sample was dispersed on a carbon film from an acetone suspension which was reinforced on a copper grid, and images were recorded at an accelerating voltage of 200 keV.

Density Measurements. The densities of all samples were measured using a Quantachrome Micropycnometer with helium as the working fluid.

Solid-State NMR. Solid state ^{119}Sn MAS NMR data were obtained at 4.7 T (^{119}Sn Larmor frequency of 76.2 MHz) using a Chemagnetics CMX-200 spectrometer. All experiments were performed using a Doty 4 mm MAS probe in which MAS frequencies of 10 kHz were implemented at ambient temperatures. A ^{119}Sn $\pi/2$ pulse time of 4 μs was measured on neat $(CH_3)_4Sn$, from which $\pi/4$ pulse times of 2 μs and recycle delays of 60 s were employed in subsequent single pulse measurements. All ^{119}Sn chemical shifts are referenced to the IUPAC primary reference $(CH_3)_4Sn$ at δ 0.0 ppm. Broadline (static) solid state ^{49}Ti NMR data were acquired at 14.1 T on the ^{49}Ti isotopically enriched pyrochlore sample and an enriched rutile TiO_2 sample as a reference (^{49}Ti Larmor frequency of 33.80 MHz) using a Bruker Avance II-600 spectrometer. These measurements were performed using a Bruker 5 mm static probe at ambient temperatures. A ^{49}Ti "nonselective" (solution) $\pi/2$ pulse time of 16 μs was measured using a neat $TiCl_4$ solution, which corresponds to a "selective" $\pi/2$ pulse time (for a spin I = 7/2 nucleus) of 4 μs. Subsequent ^{49}Ti data was acquired using a solid echo θ - τ - θ - τ - (acquire) ($\theta = \pi/4$ or 2 μs) experiment with an extended phase cycle to capture undistorted echoes with minimal influences from residual echo tails and finite pulse width effects,[24] and recycle delays of 2−5 s. All ^{49}Ti chemical shifts were referenced to the IUPAC primary reference $TiCl_4$ at δ 0.0 ppm. All reported ^{49}Ti chemical shifts δ are "apparent" shifts and are uncorrected for second order quadrupole effects unless specifically designated as isotropic chemical shifts δ_{iso}. All simulation and fitting of the ^{49}Ti data were performed with the DMFIT software package.[25]

Neutron Scattering. Total neutron scattering experiments were performed using the GEM[26] diffractometer at ISIS, the U.K. spallation neutron source. Powdered samples were packed in vanadium cans with inner diameter 7.62 mm and wall thickness 0.13 mm, and data were accumulated for approximately 5 h from each to ensure good statistical quality. Data were also collected from an empty vanadium can, the empty instrument, and an 8.34 mm diameter vanadium rod for normalization. The programs Gudrun[27] and ATLAS[28] were used to correct the data and to produce the distinct scattering, $i(Q)$,

$$i(Q) = I(Q) - I^S(Q) \quad (1)$$

dx.doi.org/10.1021/cm202908s | Chem. Mater. 2011, 23, 5464−5473

where Q is the magnitude of the scattering vector, $I(Q)$ is the corrected total scattering, and $I^S(Q)$ is the (incoherent) self-scattering, which can be calculated within an approximation.[28]

The differential correlation function, $D(r)$, was obtained by the standard approach[29] of Fourier transformation of $i(Q)$, in this case with Q_{max} = 20 Å^{-1} and using the Lorch modification function, $M(Q)$,[30]

$$D(r) = \frac{2}{\pi}\int_0^{Q_{max}} Q\ i(Q)\ M(Q)\ \sin rQ\ dQ \quad (2)$$

The function $D(r)$ is hereafter referred to as the pair distribution function (PDF). Analysis of the neutron diffraction pattern was carried out on the data from GEM detector bank 3 (mean scattering angle 34°) using the program GSAS[31] and pair distribution function analysis was carried out on data from a combination of detector banks using the program PDFgui.[32] In PDFgui the goodness of fit is defined as using a standard weighted residual:

$$wR = \left(\frac{\sum |w|Y_O - Y_C|^2|}{\sum |wY_O^2|}\right)^{1/2} \quad (3)$$

Where Y_O and Y_C are the observed and calculated values, respectively, the weight, w, is the reciprocal of the square of the standard deviation of the data point.

TPR and Catalysis. TPR experiments were performed at Johnson Matthey Technology Centre, Sonning Common, Reading, U.K., using an in-house designed rig. The TPR experiments involved passing a 10% H_2 in N_2 gas mixture over the sample and measuring the thermal conductivity of the gas mixture after passing over the sample using a thermal conductivity detector. Initially a known amount of the gas mixture was injected into the system to act as a calibration peak to determine the amount of hydrogen consumed by the sample after the experiment. The sample was heated at a rate of 10 °C min^{-1} to 773 K, and then reoxidized using a TPO by a similar method but using a 10% O_2 in He gas mixture to 523 K. The data were analyzed by integration and comparison of the sample peak to the calibration peak. To study WGS activity, Au-loaded pyrochlore catalyst was prepared by hydrolysis deposition. Pyrochlore (9.6 g) was slurried in water (400 cm^3) and warmed to 60 °C. The pH was adjusted to 8.0 by the addition of sodium carbonate solution (0.05 M). $HAuCl_4$ (0.39 g, 49.24 wt % Au) was dissolved in water (75 cm^3) and pumped into the stirred support slurry at about 10 cm^3 min^{-1}. The pH was monitored throughout, and base (Na_2CO_3, 0.05 M) was pumped in at variable rate to maintain the pH as close as possible to 8.0 throughout the gold addition. This was achieved using a 3-term PID controller with feedback loop to the pH probe. After the gold addition was complete, stirring was continued for a further 1 h. The catalyst sample was recovered by filtration, thoroughly washed to remove soluble chloride, and oven-dried at 105 °C. Au deposition was not quantitative since assay revealed 1.3% Au by mass. For comparison, a high surface area (HSA) CeO_2 sample with a comparable surface area to the pyrochlore sample (HSA5, supplied by Rhodia: surface area ~100 m^2 g^{-1}) was prepared identically to give the same gold loading. A glass reactor charged with catalyst was placed inside the furnace on a catalyst testing rig built at the Johnson-Matthey Technology Centre. The furnace and surrounding pipe work was contained in an oven, which was kept at 110 °C to prevent water condensation. Gases were supplied via mass flow controllers, and water was pumped into a steam pot at the required rate via a peristaltic pump. A four-way valve arrangement enabled either inlet or outlet gas samples to be directed to the analyzers. Catalyst samples were pelletized, crushed, and then sieved to between 250−355 μm particle size prior to testing. The test conditions were as follows: 30% H_2O, 5% CO with balance N_2. The space velocity was 40,000 cm^3 g^{-1} h^{-1}. In a typical test the catalyst charge was 0.45 g and the total flow 300 cm^3.

RESULTS AND DISCUSSION

1. Structure. Our initial structural description of the material with idealized composition $(Na_{0.33}Ce_{0.67})_2Ti_2O_7$ was based on powder diffraction analysis, which showed a crystalline pattern that could be indexed on a face-centered cubic unit cell (a = 10.120(9) Å) with peak intensities that matched well the assumed chemical formula and assuming a stoichiometric pyrochlore structure.[22] The ideal $Fd\bar{3}m$ pyrochlore $A_2B_2O_7$ structure may be thought of as an anion-deficient fluorite structure with oxide-ion vacancies ordered in such a way as to reduce the coordination number of one-half of the metal sites from eight to six: this gives two types of oxide positions, the 48f site, which bridges both the A and B metal sites and the 8b site, which is coordinated only to A sites (using a cell setting with the B metal placed at the origin).[33] Our formulation $(Na_{0.33}Ce_{0.67})_2Ti_2O_7$ was supported by XANES analysis at the Ce L_{III} and Ti K edges that showed the presence of solely cerium(IV) and titanium(IV),[23] and thus charge balance is maintained by the presence of sodium on the A-site as well as full occupation of the pyrochlore 8b site with O^{2-} in this simple model. In addition, the ratio of A and B site ionic radii (using the weighted average values of Na^+ and Ce^{4+} for the A site[34]) is 1.58, indicating that this composition is reasonable for a cubic $A^{3+}{}_2B^{4+}{}_2O_7$ pyrochlore, based on "stability fields" analyzed by Subramanian et al.[33]

Before more detailed structure analysis was undertaken, thermodiffractometry experiments were performed in air to examine the thermal stability of the pyrochlore, Figure 1. These

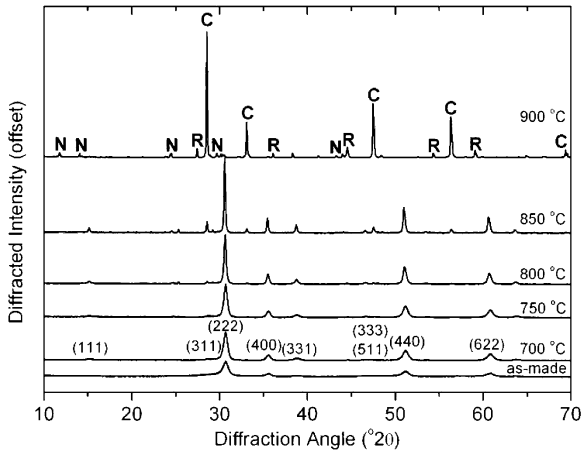

Figure 1. Powder XRD patterns measured at room temperature and after annealing the sodium cerium titanate pyrochlore at various temperatures. The Miller indices of the $Fd\bar{3}m$ pyrochlore unit cell (a = 10.120(9) Å) are shown. For the phase-separated sample, the most intense Bragg peaks due to CeO_2, rutile TiO_2 and $Na_2Ti_6O_{16}$ are labeled **C**, **R**, and **N**, respectively.

show that on heating to 700 °C the pyrochlore structure is maintained, and indeed crystallinity is increased with the weak (111) reflection at $2\theta \sim 15°$ becoming apparent on annealing. On further heating, however, the formation of CeO_2, TiO_2 (rutile polymorph), and $Na_2Ti_6O_{13}$[35] is apparent, and after heating at 900 °C under these conditions the sample is almost completely decomposed into the simpler oxide phases. TEM images before and after heating, Figure 2, show an increase in crystallite size from less than 10 nm diameter to greater than 20 nm diameter, and on heating at 850 °C, larger rod-shaped crystallites are also seen, which are most likely to be the CeO_2

dx.doi.org/10.1021/cm202908s | Chem. Mater. 2011, 23, 5464−5473

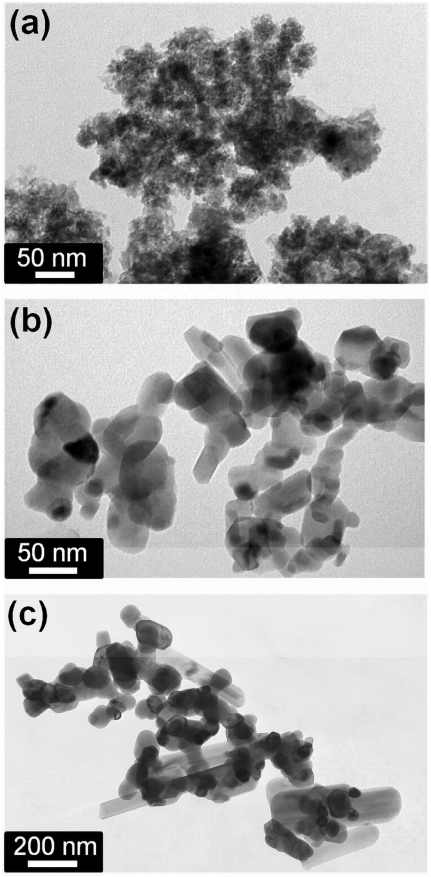

Figure 2. TEM images of the sodium cerium titanate pyrochlore (a) as-made (b) after annealing at 700 °C and (c) after annealing at 850 °C.

formed on collapse of the pyrochlore. TGA-DSC of the as-made material, isolated by filtration and dried at 70 °C in air, shows a considerable amount of surface water (around 7.5% by mass, see Supporting Information), but this is removed completely on heating the material at 300 °C in air for 5 h without any apparent collapse of the pyrochlore phase.

Owing to the broadened XRD profile, which may be ascribed largely to small crystallite size, refinement of structure from conventional X-ray diffraction data is problematic. This is especially true because full structure refinement of pyrochlores is complicated since the structure may contain various types of disorder, including oxide-ion deficiency, oxide-ion excess, migration of oxide ions to give fluorite-like order and occupation of the 8*b* oxide site by other anions (such as hydroxide or halide) or by water, all of which may be rather difficult to detect in the X-ray diffraction experiment because heavy metals dominate the scattering.[33] For our material, we also noticed that successful synthesis always required an excess of titanium: Ce/Ti of 1:2.5 instead of 1:1.49 implied by the ideal chemical formula. Furthermore, the measured density of the sample dried at 300 °C was notably lower (4.912 g cm^{-3}) than the value expected for the assumed chemical formula (5.288 g cm^{-3}). To understand these issues, to build a more complete picture of the structure of the pyrochlore material and in doing so determine its true composition, we have therefore used total neutron scattering. We studied two samples: one that had been thermally annealed in air at 300 °C to remove water and hence eliminate incoherent scattering from hydrogen in the neutron experiment, and one that had been annealed at 700 °C to provide a more crystalline sample to aid analysis. Figure 3a

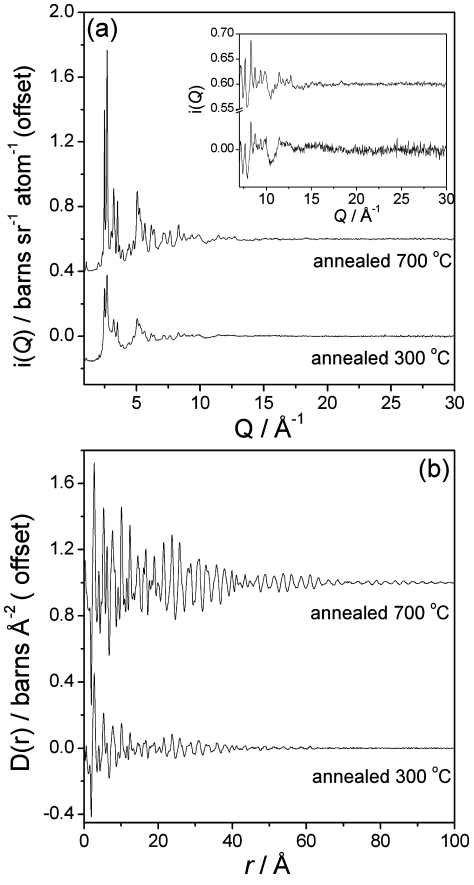

Figure 3. (a) $i(Q)$ for the two pyrochlore samples studied with an inset showing an expanded region of the high Q region and (b) $D(r)$ for the two samples.

shows $i(Q)$ measured for the two samples. The sample annealed at 700 °C shows weak, broad Bragg peaks of poorly crystalline CeO_2 (see below), of which all but the strongest, the (022) peak at d = 1.92 Å, are not apparent for the 300 °C sample, and this impurity may have resulted from the onset of the thermal collapse of the material. The effect of the smaller particle size in the sample treated at lower temperature is obvious in the radial distribution functions produced by Fourier transformation of the scattering data, with a more rapid damping of the information in the PDF with increasing r (Figure 3b). To simulate the PDFs generated from the scattering data, we built an initial model based on the simple cubic pyrochlore structure, assuming the idealized composition $(Na_{0.33}Ce_{0.67})_2Ti_2O_7$. Figure 4a shows the fit of this model to the PDF for both samples studied: this was achieved after refining the lattice parameter and the x coordinate of the 48*f* oxygen (the only two crystallographic variables of the $Fd\bar{3}m$ pyrochlore), along with isotropic thermal displacement parameters and the "spherical particle diameter" parameter which models the damping of the PDF due to small crystal size.[32]

Although the ideal cubic pyrochlore structure fits the observed PDF in general form, with the positions of peaks and troughs well matched, there are clear deficiencies in this simple model, most apparent in the short-range distance region

dx.doi.org/10.1021/cm202908s | *Chem. Mater.* 2011, 23, 5464–5473

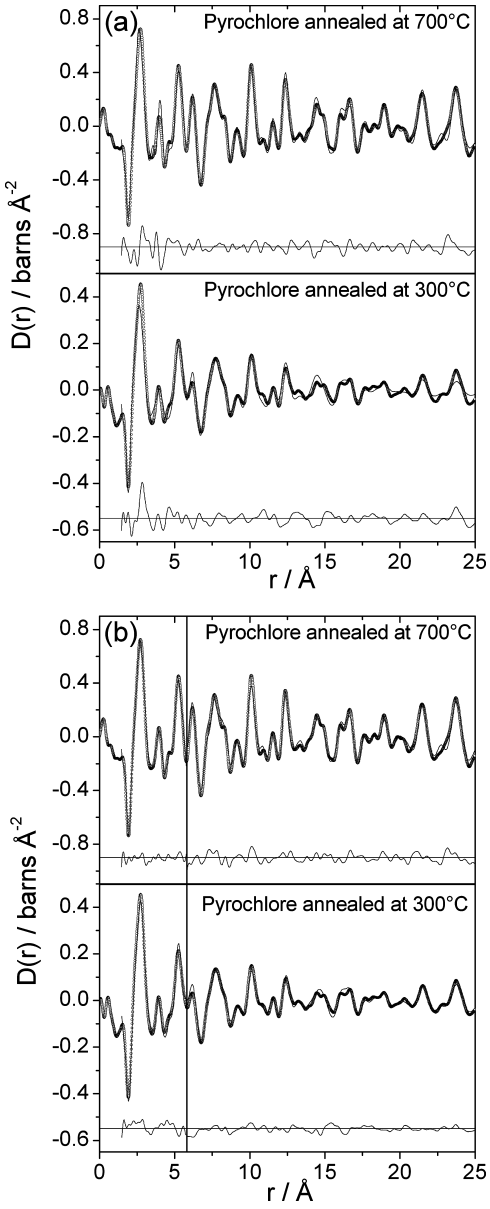

Figure 4. Fits to the PDF for two samples studied: (a) cubic $Fd\bar{3}m$ pyrochlore model with composition $(Na_{0.33}Ce_{0.67})_2Ti_2O_7$ and (b) final refined model $(Na_{0.33}Ce_{0.53}Ti_{0.14})_2Ti_2O_7$ with short-range order (<5.8 Å, denoted by the vertical line) modeled with symmetry $F\bar{4}3m$. Circles are data points, the thin line the total fit from the model, and the gray lines below each PDF are difference traces. See Supporting Information for a magnified plot of the low r region of these plots.

of the patterns. First, the intensities of the first two peaks in the PDF, which correspond to B−O correlations, and a combination of A-O and O--O correlations (corresponding to the closest approach of 48*f* site oxide ions), respectively, are not well matched, and second, the region 3.5−5 Å shows mismatch in intensities. To refine the model, three points were considered; (i) the neutron scattering lengths of the elements in this material give excellent contrast with respect to Ti to allow the actual composition of the sample to be refined (coherent values of scattering lengths for natural isotope mixtures are Na, 3.63 fm, Ce, 4.84 fm, Ti −3.438 fm, and O, 5.803 fm[36]) so this should provide a starting point for correcting the discrepancy in intensity of B-O and A-O peak intensities, (ii) the small amount of poorly crystalline CeO_2 seen in the Bragg scattering of the samples should be added to the model, and (iii) inspection of the partial pair distribution functions (Supporting Information) shows that the discrepancies seen around 4 Å are mostly likely due to O--O nonbonded distances and A--O second nearest neighbor correlations. The last point required various possibilities of disorder in the pyrochlore structure to be considered, including oxide ion deficiency (partial occupation of the 8*b* site), oxide ion excess (occupation of the 8*a* site at the expense of the 48*f* site) and crystallographic models of lower symmetry that provide variability in the position of the 48*f* oxide ions. Removal or addition of oxide ions (with adjustment of the Na/Ce ratio to maintain charge balance) always gave significantly poorer fits to the PDF, and hence models that allowed displacement of oxide ions were considered. Lowering of symmetry to $F\bar{4}3m$ allows variability in the position of what was the $Fd\bar{3}m$ 48*f* oxygen (i.e., the oxygen that bridges between the A and B sites) and has previously been observed in pyrochlores including those with oxygen excess, such as $Ce_2Zr_2O_{7.5}$,[37] oxygen deficiency, such as $Pb_2Ru_2O_{6.5}$,[38] and those with stoichiometric composition, such as Y-doped $Bi_2Sn_2O_7$.[39] This approach allowed the discrepancies in the PDFs in O--O and A---O correlations for our material to be removed. It is important to note, however, that the Bragg diffraction (see below) shows no extra peaks associated with this lowering of symmetry, suggesting that the oxide-ion displacement from the ideal cubic pyrochlore structure occurs only on a local scale. Therefore, we modeled the PDF in two parts: the local structure using the $F\bar{4}3m$ model (until 5.8 Å, a convenient point in the PDF that lies in a trough) and the longer range structure using the $Fd\bar{3}m$ model. In addition, a small amount of CeO_2 was added as an impurity phase, and finally the occupancy of the A-site was refined to explore the possibility of excess Ti^{4+}, to be consistent with the extra Ti used in synthesis. The amount of A-site titanium always refined away from zero and converged on a value of close to $x = 0.14$ (the mean value from the refinements of each sample) for an A site expressed as $Na_{0.33}Ce_{0.67-x}Ti_x$. The final fits to the PDFs are shown in Figure 4b with refined parameters contained in Tables 1 and 2. For both materials studied, their agreement factors, *wR*, for the final model were lower than for the simple pyrochlore model.

Figure 5a shows the low r region of the PDF for the sample annealed at 700 °C, which illustrates the need for inclusion of excess titanium in the structural model. The refined amount of the pure CeO_2 impurity phase for the sample annealed at 700 °C was found to be 6.7% weight percent, while for the sample annealed at lower temperature a value of 2.0% was found. We found no evidence for the presence of any polymorph of TiO_2 in either sample. In the standard $Fd\bar{3}m$ pyrochlore model, the oxygen 48*f* site x-coordinate must fall within the range 0.3125−0.375, with the end values representing perfectly regular B and A sites, respectively. The refined x-coordinates of the two 24-fold oxygen sites in the $F\bar{4}3m$ local-structure model are 0.296 and 0.062, which would correspond to a mean 48*f* x-coordinate of 0.321 in the $Fd\bar{3}m$ model. This implies, therefore, that the B site is, on average, close to regular octahedral, while the A site is distorted cubic. Using the $F\bar{4}3m$ local structure model, the bond valence sum[40] for the B-site titanium is 4.1(1). The local environment of the A-site is more complicated: our model involves a random occupation of this site by three elements Na, Ce, and Ti, and therefore it is not unexpected that an average structural distortion is seen with a range of A-O distances from

dx.doi.org/10.1021/cm202908s | *Chem. Mater.* 2011, 23, 5464−5473

Table 1. Final Fitted Parameters from PDF Analysis of Pyrochlore Samples Annealed at 300 and 700 °C Using the Ideal $Fd\bar{3}m$ Model[a]

	$Fd\bar{3}m$ pyrochlore model (700 °C sample)	$Fd\bar{3}m$ pyrochlore model (300 °C sample)
a / Å	10.1162(7)	10.1292(4)
A site ADPs	*U*11 = 0.0115(6)	*U*11 = 0.0247(4)
*U*11 = *U*22 = *U*33, *U*12 = *U*13 = *U*23	*U*12 = 0.0032(5)	*U*12 = −0.0029(4)
B site ADPs	*U*11 = 0.0196(8)	*U*11 = 0.0343(6)
*U*11 = *U*22 = *U*33, *U*12 = *U*13 = *U*23	*U*12 = −0.0017(5)	*U*12 = −0.0080(4)
O 48f site ADPs	*U*11 = 0.0292(6)	*U*11 = 0.0366(4)
*U*11, *U*22 = *U*33, *U*23	*U*22 = 0.0261(4)	*U*22 = 0.0373(3)
	*U*23 = 0.0128(8)	*U*23 = 0.0239(4)
O 8b site ADPs	*U*11 = 0.0231(6)	*U*11 = 0.0174(3)
*U*11 = *U*22 = *U*33		
A site Ti occupancy	0.127(8)	0.149(2)
O 48*f* site *x*-coordinate	0.3253(1)	0.3279(6)
CeO_2content (%)	6.7	2.0
R_w	0.188	0.230

[a]For comparison the model with no excess titanium and lacking CeO_2 gave R_w values for 700°*C* = 0.217, 300°*C* = 0.276.

Table 2. Final Fitted Parameters from PDF Analysis of Pyrochlore Samples Annealed at 300 and 700 °C Using the $F\bar{4}3m$ Local-Structure Model at <5.8 Å

	$F\bar{4}3m$ local structure model (700 °C sample)	$F\bar{4}3m$ local structure model (300 °C sample)
a / Å	10.2050(6)	10.2042(7)
fractional coordinates		
16*e* (A site)	*x* = *y* = *z* = 0.86795(5)	*x* = *y* = *z* = 0.8646(1)
16*e* (B site)	*x* = *y* = *z* = 0.38292(5)	*x* = *y* = *z* = 0.3760(1)
24*f*	*x* = 0.29696(8), *y* = *z* = 0	*x* = 0.2911(1), *y* = *z* = 0
24*g*	*x* = 0.06180(5), *y* = *z* = 0.25	*x* = 0.06013(6), *y* = *z* = 0.25
4*a*	*x* = *y* = *z* = 0	*x* = *y* = *z* = 0
4*d*	*x* = *y* = *z* = 0.75	*x* = *y* = *z* = 0.75
A site ADPs	*U*11 = 0.0838(4)	*U*11 = 0.0326(7)
*U*11 = *U*22 = *U*33, *U*12 = *U*13 = *U*23	*U*12 = −0.0396(2)	*U*12 = −0.0136(6)
B site ADPs	*U*11 = 0.00408(8)	*U*11 = 0.0088(4)
*U*11 = *U*22 = *U*33, *U*12 = *U*13 = *U*23	*U*12 = 0.0027(1)	*U*12 = 0.0088(3)
O 24f site ADPs	*U*11 = 0.0114(1)	*U*11 = 0.0062(4)
*U*11, *U*22 = *U*33, *U*23	*U*22 = 0.0237(2)	*U*22 = 0.094(2)
	*U*23 = −0.0109(2)	*U*23 = −0.061(2)
O 24 g site ADPs	*U*11 = 0.0139(2)	*U*11 = 0.0045(2)
*U*11, *U*22 = *U*33, *U*23	*U*22 = 0.0197(1)	*U*22 = 0.0172(3)
	*U*23 = 0.0082(2)	*U*23 = 0.0074(5)
O 4a site ADPs	*U*11 = 0.0063(1)	*U*11 = 0.0119(3)
*U*11 = *U*22 = *U*33		
O 4d site ADPs	*U*11 = 0.189(1)	*U*11 = 0.1[a]
*U*11 = *U*22 = *U*33		
R_w	0.055	0.110

[a]Note that this value was not refined because doing so caused instability.

~2.0 Å to ~2.6 Å (see Supporting Information for bond distances). The bond valence sum for the A-site cerium therefore has no physical significance.

Figure 5b shows a comparison of the neutron Bragg scattering for the sample annealed at 700 °C with the patterns

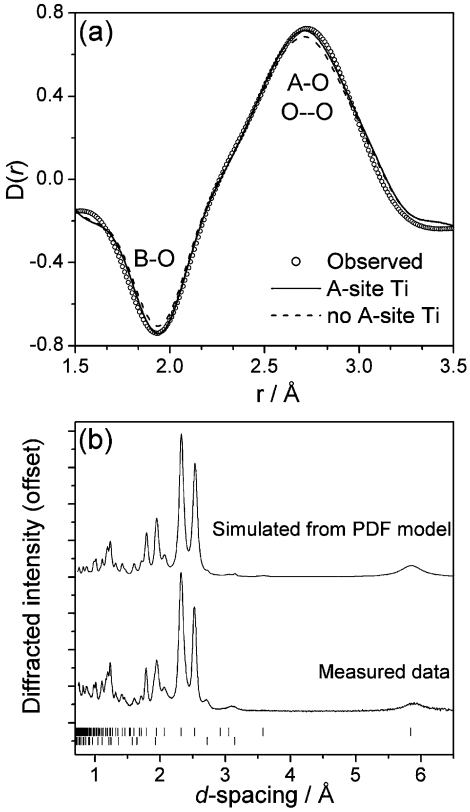

Figure 5. (a) Low *r*-region of PDF showing effect of excess Ti on the fit and (b) comparison of observed Bragg diffraction with that simulated from the final structural model derived from PDF analysis for the sample annealed at 700 °C. Tick marks are for the $Fd\bar{3}m$ pyrochlore structure (upper) and CeO_2 (lower).

simulated using the PDF-derived structural models (peak broadening parameters were obtained by an initial Le Bail fit of the Bragg profile). The calculated density for our new average structural model is 4.95 g cm^{-3} (including the ceria impurity) which shows good agreement with the measured value of 4.91 g cm^{-3} for the sample annealed at 300 °C: for comparison, the calculated value for the ideal cubic pyrochlore with no excess titanium is 5.29 g cm^{-3}. Thus we have deduced a composition and structural model for the pyrochlore phase, consistent with all experimental observations. For the material as-prepared the chemical formula $(Na_{0.33}Ce_{0.53}Ti_{0.14})_2Ti_2O_7{\cdot}1.75H_2O$ takes into account the surface 7.5% water seen by TGA. The extra A-site titanium is not unreasonable: in a range of other pyrochlore oxides the presence of an intended B-site metal on the A-site has been detected,[41] including in some reduced lanthanide titanates.[42] It is likely that the small amount of A-site Ti is actually displaced off-center from the pyrochlore A-site, but with the small amount of Ti on the A-site in our material, it proved to be too low to refine meaningfully the model further against the present data.

Further corroboration and insight into the local structure of the pyrochlore phase was obtained using ^{49}Ti solid state NMR of an enriched sample. An unfortunate feature of Ti NMR is the very near coincidence of the ^{47}Ti and ^{49}Ti chemical shift ranges which complicates the experimental interpretation, and recourse to complete isotopic substitution by either the ^{47}Ti or the ^{49}Ti nucleus (incorporated as a precursor in the synthesis route) is often necessary to assist the NMR study. The spectrum of the ^{49}Ti-enriched pyrochlore, Figure 6a, shows that

dx.doi.org/10.1021/cm202908s | *Chem. Mater.* 2011, 23, 5464–5473

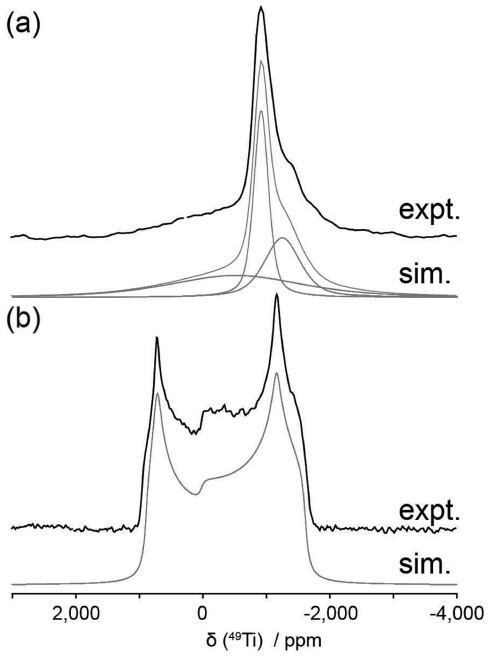

Figure 6. ^{49}Ti NMR of (a) the enriched sodium cerium titanate pyrochlore and (b) the enriched rutile TiO_2. In (a) the simulation of the signal as three distinct resonances is shown.

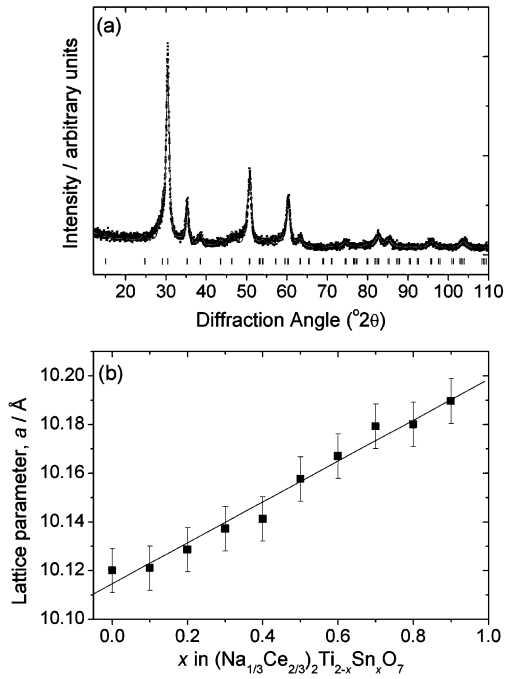

Figure 7. Powder XRD analysis of tin-doped pyrochlores (a) profile fit to the sample with maximum Sn content (Sn:Ti = 0.4:0.6), where the points are the observed data, the line the fit, and the tick marks those for the $Fd\bar{3}m$ unit cell and (b) dependence of lattice parameters on composition.

two ^{49}Ti resonances from this phase are observable. The dominant resonance at an apparent shift of δ −912 ppm may be assigned to the B-site, six-coordinate titanium, whereas the smaller feature with an upfield apparent shift of δ −1245 ppm is consistent with the presence of some A-site titanium, as seen in the neutron scattering studies. These resonances sit on top of a background consisting of some ^{49}Ti satellite excitation ($\pm 1/2 \leftrightarrow \pm 3/2$, $\pm 3/2 \leftrightarrow \pm 5/2$, $\pm 5/2 \leftrightarrow \pm 7/2$ for spin $I = 7/2$) and unincorporated ^{49}Ti present in the form of disordered TiO_2 (rutile) present as a consequence of the synthesis. This spectrum is compared with that obtained for highly crystalline rutile, Figure 6b, which is characterized by a very broad second order quadrupolar line shape. The simulation of this line shape affords the elucidation of the following NMR interaction parameters (δ_{iso} 4.06 ppm, C_Q = 13.02 MHz, η = 0.16) assuming that only a quadrupole broadening is contributing to the line width. These results compare well against previously reported values from lower field (9.40 T) measurements on natural abundance/unresolved ^{47}Ti and ^{49}Ti systems, which are disadvantaged by a potential for lower intrinsic accuracy.[43] A direct comparison of the spectra in Figure 6 clearly demonstrates that the ^{49}Ti linewidths (full width half-maximum) measured for $(Na_{0.33}Ce_{0.53}Ti_{0.14})_2Ti_2O_7 \cdot 1.76H_2O$ are approximately an order of magnitude less than that of rutile. The narrow line width of the B-site pyrochlore resonance is consistent with a high point symmetry exhibited by titanium, suggesting little distortion from the ideal octahedron; nevertheless, both sites in the pyrochlore show evidence of additional disorder broadening which corroborates the displaced oxide anion model accommodating the local disorder.

2. Tin-Doped Materials. The materials doped with tin were studied using powder X-ray diffraction: Figure 7a shows a typical profile refinement and Figure 7b the cubic lattice parameter as a function of tin content. The expansion of the lattice is consistent with the replacement of a proportion of octahedral Ti(IV) (r = 0.745 Å[34]) with Sn(IV) (r = 0.83 Å[34]), as also seen in Sn-doped TiO_2, for example.[44] As might be expected, the magnitude of the lattice expansion is rather less for the more complex oxide than for the rutile solid solution, and interestingly for the pyrochlore we see an approximately linear relationship between lattice parameter and tin content, whereas in the $Ti_{1-x}Sn_xO_2$ system a positive deviation from Vegards' Law is observed.[44] Note that since we only studied the doped materials by laboratory X-ray diffraction we have not made a detailed analysis of their local structure. The maximum tin content was found to be Ti:Sn = 0.6:0.4: above this value hydrothermal reactions produced crystalline SnO_2 as a byproduct. The presence of Sn(IV) in the doped pyrochlore was confirmed using ^{119}Sn solid-state NMR, Figure 8, which shows a broad feature with an average chemical shift of δ −680 ppm characteristic of octahedral Sn(IV): for comparison, the related (also diamagnetic) materials $La_2Sn_2O_7$, $Y_2Sn_2O_7$, and $Lu_2Sn_2O_7$ that all contain octahedral, B-site Sn(IV) show shift values of δ −642, δ −582, and δ −641 ppm, respectively.[45] The isotropic chemical shift of ^{119}Sn in SnO_2, which contains a distorted octahedral environment, is δ −610 ppm.[46] The absence of spinning side bands in our spectra confirms the high symmetry of the Sn site, suggesting only B-site Sn(IV), but we note the very broad signals seen in the NMR spectra for our materials: this can be ascribed to the variety of next-nearest neighbor interactions in a multielement system, giving a range of unresolved chemical shifts, as has been recently reported in the phase $Y_2Ti_{2-x}Sn_xO_7$.[47]

3. TPR. Figure 9 shows TPR/TPO traces for the parent pyrochlore material (note this experiment was performed on the material without supported precious metals). After an initial cycle of reduction followed by reoxidation, the material exhibits a low temperature reduction peak, centered at 158 °C. After the second reoxidation, the third reduction cycle shows that the

dx.doi.org/10.1021/cm202908s | Chem. Mater. 2011, 23, 5464–5473

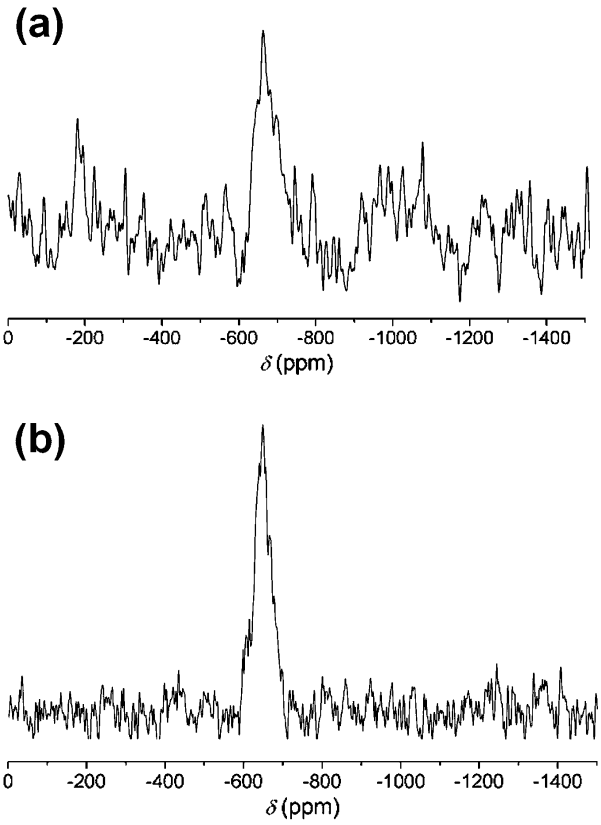

Figure 8. ^{119}Sn NMR measured from (a) 10% tin-doped sample and (b) 40% tin-doped sample.

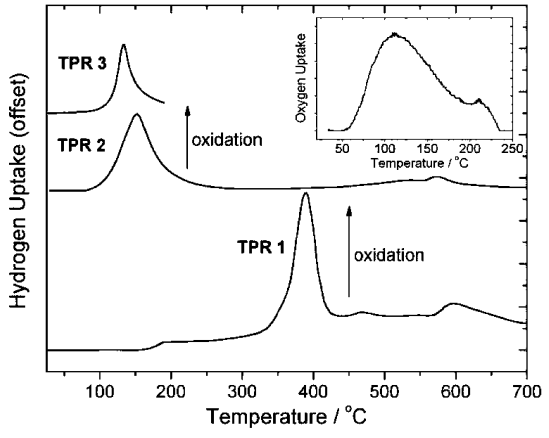

Figure 9. TPR profile of $(Na_{0.33}Ce_{0.53}Ti_{0.14})_2Ti_2O_7$ pyrochlore over three cycles. Intermittent mild reoxidation was applied between the TPR runs by heating in 5% O_2 in He to 250 °C: the inset shows the TPO trace after the first TPR.

low temperature reduction properties are maintained. Table 3 summarizes the TPR data. It should be noted that although the reoxidation steps were carried out using a temperature-programmed O_2/He flow up to 250 °C, after reduction we in fact found that exposure to air at ambient temperature is sufficient for reoxidation. The first "activation" step we observe, before the low temperature reduction is seen (i.e., TPR1 followed by mild oxidation), might be attributed to surface water from the as-made material, which was seen by TGA. It is also worth noting that similar activation cycles (described as redox cycle aging) have been reported to be necessary to

Table 3. Summary of TPR Results for $(Na_{0.33}Ce_{0.53}Ti_{0.14})_2Ti_2O_7$

TPR cycle	reduction onset (°C)	main reduction peak center (°C)	hydrogen uptake (mmol [H] g^{-1})	cerium reduced (%)
1	175	390	1.81	72
2	94	158	1.78	71
3	94	128	1.75	70

optimize the redox properties of ceria-zirconia materials,[48] and for those it has been proposed that either cerium clustering at the surface of the particles or an increase in oxide-ion defect sites is responsible for the enhanced reducibility after redox cycling. The powder XRD after the second TPR cycle (Supporting Information) shows that the average pyrochlore structure is maintained, with no indication of the formation of CeO_2: all Bragg peaks can be indexed on the expected $Fd\bar{3}m$ cubic unit cell. Consistent with the slight sharpening of the Bragg peaks seen in the XRD, TEM shows that the average particle size has increased after TPR (Supporting Information). The TPR results in Figure 9 thus show that, despite an increase in particle size (and hence a decrease in surface area), the redox properties are improved after the initial TPR-TPO cycle. This strongly suggests that it is the pyrochlore structure of the material that is responsible for the redox activity, rather than the high surface area of the as-made nanocrystalline material. Once "activated", the pyrochlore shows reversible reduction at considerably lower temperature than high surface area ceria which has been studied by many researchers: CeO_2 itself is well-known to show characteristic surface reduction with maximum uptake at ~500 °C followed by bulk reduction at >800 °C.[49]

Figure 10a shows TPR of a tin-doped sample (10% Sn). The TPR experiment was carried out to below 500 °C since we

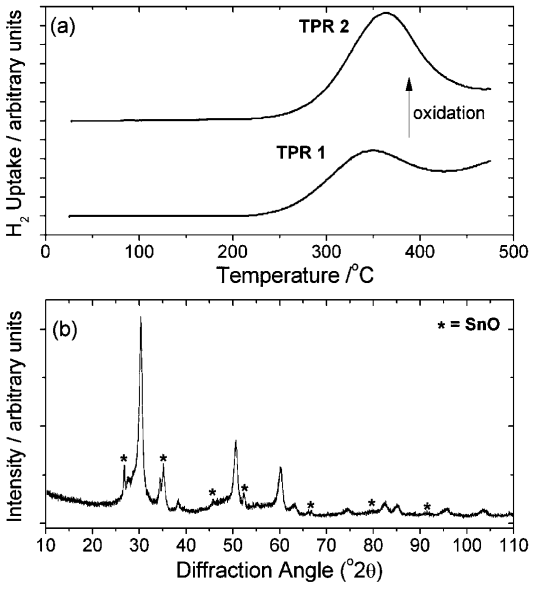

Figure 10. (a) TPR of Sn-doped sample and (b) XRD after TPR to 900 °C showing phase separation of the sample to SnO.

observed that no recyling was possible if performed to higher temperatures. The main reduction feature here is observed at 350 °C, and this is then reproducible after subsequent reoxidation. The lower temperature of the initial reduction

dx.doi.org/10.1021/cm202908s | Chem. Mater. 2011, 23, 5464–5473

compared to the parent material may reasonably be ascribed to the expanded lattice, giving high oxide-ion mobility. The tin-doped samples are, however, susceptible to collapse under reducing conditions: Figure 10b shows powder XRD of the sample after heating to 900 °C in the TPR experiment, showing that phase separation to SnO has taken place. The rather different coordination geometry preferred by Sn(II) would explain why it is not possible to recycle this material once it has collapsed.

4. Application in WGS Catalysis. Figure 11 shows the WGS catalysis results from a sample of the parent pyrochlore loaded with gold, showing the CO conversion with temperature in comparison with a reference high surface area ceria (also supporting gold). The pyrochlore clearly shows higher activity than the ceria reference, with 50% CO conversion achieved at ~50 °C below CeO_2. Comparison with recent literature studies of ceria solids is also informative: our results for gold on HSA-CeO_2 are similar to those reported by Fu et al.,[50] whereas Kušar et al. studied CuO-CeO_2 materials and found up to 60% conversion at ~500 °C and also reported data for a commercial CuO-ZnO-Al_2O_3 material that show an equilibrium CO conversion of ~80% at around 200 °C,[18] and Germani and Schuurman studied Pt/CeO_2/Al_2O_3 catalysts within a stainless-steel microchannel reactor and found around 80% conversion of CO at 300 °C.[51] It must be noted that when comparing results from previous studies, we have used only CO and H_2O mixtures as the feed gas (rather than reformate mixtures) and that no standard space velocity has previously been used, but nevertheless the pyrochlore material activated with gold shows high WGS activity comparable to typical highly active catalysts.

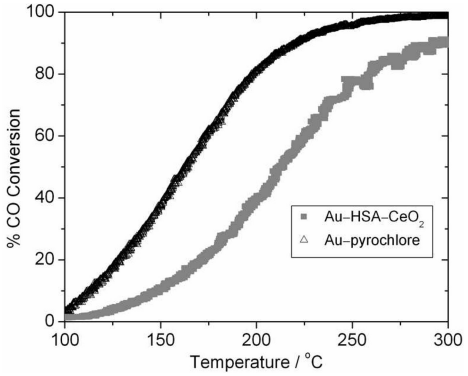

Figure 11. WGS results expressed as percentage CO conversion for gold-loaded $(Na_{0.33}Ce_{0.53}Ti_{0.14})_2Ti_2O_7$ pyrchlore and gold-loaded high surface area (HSA) ceria.

CONCLUSIONS

We have produced a refined structural model for a sodium cerium titanate pyrochlore material, using neutron PDF analysis and solid-state NMR, which provides details of local disorder and that is consistent with all other experimental observations. Doping is possible in one-step hydrothermal reaction to yield complex mixed-metal oxides. It is important to note that the presence of sodium and titanium along with cerium on the pyrochlore A-site does not affect the reducibility of cerium(IV): the TPR shows that around 75% of the cerium can be reduced reversibly at lower temperatures than ceria itself. The thermal instability of the pyrochlore phase at high temperatures shows how its synthesis would be difficult, if not impossible, by conventional solid-state methods, or even by sol–gel processing, which requires annealing to induce crystallinity. The thermal collapse at high temperatures may also be an issue for practical applications, but as we have shown using water gas shift as an example, important low temperature catalysis applications can make use of the ease of reduction of cerium(IV) in the pyrochlore lattice.

ASSOCIATED CONTENT

Supporting Information

Further details about TGA-DSC results (Figure S1.1), neutron scattering results (Figures S2.1–S2.3, Table S2.1), and analysis of pyrochlore after TPR experiments (Figures S3.1 and S3.2). This material is available free of charge via the Internet at http://pubs.acs.org.

AUTHOR INFORMATION

Corresponding Author

*E-mail: r.i.walton@warwick.ac.uk.

ACKNOWLEDGMENTS

We are grateful to EPSRC for the award of DTA studentship to D.R.M., the STFC for provision of beamtime at ISIS and for part-funding a studentship for H.Y.P. via its Centre for Materials Physics and Chemistry (Grant CMPC08104), and Johnson Matthey plc for providing additional funding. Steve York (Department of Physics, Warwick) is acknowledged for the TEM images. Some of the equipment used in materials characterization at the University of Warwick was obtained through the Science City Advanced Materials project "Creating and Characterising Next Generation Advanced Materials" with support from Advantage West Midlands (AWM) and part funded by the European Regional Development Fund (ERDF).

REFERENCES

(1) *Catalysis by Ceria and Related Materials*; Trovarelli, A., Ed.; Imperial College Press: London, 2002; Beckers, J.; Rothenberg, G. *Green Chem.* **2010**, *12*, 939. Beckers, J.; Gaudillere, C.; Farrusseng, D.; Rothenberg, G. *Green Chem.* **2009**, *11*, 921.
(2) Kašpar, J.; Fornasiero, P.; Graziani, M. *Catal. Today* **1999**, *50*, 285.
(3) Di Monte, R.; Kašpar, J. *Top. Catal.* **2004**, *28*, 47.
(4) Hilaire, S.; Wang, X.; Luo, T.; Gorte, R. J.; Wagner, J. *Appl. Catal., A* **2001**, *215*, 271.
(5) Ghenciu, A. F. *Curr. Op. Solid State Mater. Sci.* **2002**, *6*, 389.
(6) Farrauto, R.; Hwang, S.; Shore, L.; Ruettinger, W.; Lambert, J.; Giroux, T.; Liu, Y.; Ilinich, O. *Annu. Rev. Mater. Res.* **2003**, *33*, 1.
(7) Trimm, D. L.; Osnan, Z. I. *Catal. Rev. - Sci. Eng.* **2001**, *43*, 31.
(8) Trovarelli, A. *Catal. Rev. - Sci. Eng.* **1996**, *38*, 439.
(9) Ruettinger, W.; Ilinich, O.; Farrauto, R. J. *J. Power Sources* **2003**, *118*, 61.
(10) Lei, Y.; Cant, N. W.; Trimm, D. L. *Catal. Lett.* **2005**, *103*, 133.
(11) Fu, Q.; Saltsburg, H.; Flytzani-Stephanopoulos, M. *Science* **2003**, *301*, 935.
(12) Tibiletti, D.; Amieiro-Fonseca, A.; Burch, R.; Chen, Y.; Fisher, J. M.; Goguet, A.; Hardacre, C.; Hu, P.; Thompsett, D. *J. Phys. Chem. B* **2005**, *109*, 22553.
(13) Gorte, R. J.; Zhao, S. *Catal. Today* **2005**, *104*, 18. Vindigni, F.; Manzoli, M.; Damin, A.; Tabakova, T.; Zecchina, A. *Chem.—Eur. J.* **2011**, *17*, 4356. Bezen, M. C. I.; Breitkopf, C.; El Kolli, N.; Krafft, J. M.; Louis, C.; Lercher, J. A. *Chem.—Eur. J.* **2011**, *17*, 7095. Tibiletti, D.; de Graaf, E. A. B.; Teh, S. P.; Rothenberg, G.; Farrusseng, D.; Mirodatos, C. *J. Catal.* **2004**, *225*, 489.

(14) Di Monte, R.; Kašpar, J. *Catal. Today* **2005**, *100*, 27. Di Monte, R.; Kašpar, J. *J. Mater. Chem.* **2005**, *15*, 633. Baidya, T.; Hegde, M. S.; Gopalakrishnan, J. *J. Phys. Chem. B* **2007**, *111*, 5149.
(15) Sasikala, R.; Gupta, N. M.; Kulshreshtha, S. K. *Catal. Lett.* **2001**, *71*, 69. Baidya, T.; Gupta, A.; Deshpandey, P. A.; Madras, G.; Hegde, M. S. *J. Phys. Chem. C* **2009**, *113*, 4059.
(16) Wang, D. Y.; Park, D. S.; Griffith, J.; Nowick, A. S. *Solid State Ionics* **1981**, *2*, 95. Balazs, G. B.; Glass, R. S. *Solid State Ionics* **1995**, *76*, 155. Yamashita, K.; Ramanujachary, K. V.; Greenblatt, M. *Solid State Ionics* **1995**, *81*, 53. Sardar, K.; Playford, H. Y.; Darton, R. J.; Barney, E. R.; Hannon, A. C.; Tompsett, D.; Fisher, J.; Kashtiban, R. J.; Sloan, J.; Ramos, S.; Cibin, G.; Walton, R. I. *Chem. Mater.* **2010**, *22*, 6191.
(17) Baidya, T.; Gayen, A.; Hegde, M. S.; Ravishankar, N.; Dupont, L. *J. Phys.Chem. B* **2006**, *110*, 5262. Dutta, P.; Pal, S.; Seehra, M. S.; Shi, Y.; Eyring, E. M.; Ernst, R. D. *Chem. Mater.* **2006**, *18*, 5144.
(18) Kušar, H.; Hočevar, S.; Levec, J. *Appl. Catal., B* **2006**, *63*, 194.
(19) Li, G.; Smith, R. L.; Inomata, H. *J. Am. Chem. Soc.* **2001**, *123*, 11091.
(20) Roy, S.; Hegde, M. S. *Catal. Commun.* **2008**, *9*, 811.
(21) Modeshia, D. R.; Walton, R. I. *Chem. Soc. Rev.* **2010**, *39*, 4303. Riman, R. E.; Suchanek, W. L.; Lencka, M. M. *Ann. Chim.* **2002**, *27*, 15.
(22) Wright, C. S.; Fisher, J.; Thompsett, D.; Walton, R. I. *Angew. Chem., Int. Ed.* **2006**, *45*, 2442.
(23) Modeshia, D. R.; Wright, C. S.; Payne, J. L.; Sankar, G.; Fiddy, S. G.; Walton, R. I. *J. Phys. Chem. C* **2007**, *111*, 14035.
(24) Rance, M.; Byrd, R. A. *J. Magn. Reson.* **1983**, 221. Kunwar, A. C.; Turner, G. L.; Oldfield, E. *J. Magn. Reson.* **1986**, *69*, 124. Bodart, P. R.; Amoureu, J. P.; Dumazy, Y.; Lefort, R. *Mol. Phys.* **2000**, *98*, 1545. Hanna, J. V.; Pike, K. J.; Charpentier, T.; Kemp, T. F.; Smith, M. E.; Lucier, B. E. G.; Schurko, R. W.; Cahill, L. S. *Chem.—Eur. J.* **2010**, *16*, 3222.
(25) Massio, D.; Fayon, F.; Capro, M.; King, I.; Calvé, S. L.; Alonso, B.; Durand, J.-O.; Bujoli, B.; Gan, Z.; Hoatson, G. *Magn. Reson. Chem.* **2002**, 70.
(26) Williams, W. G.; Ibberson, R. M.; Day, P.; Enderby, J. E. *Phys. B* **1998**, *241−243*, 234. Hannon, A. C. *Nucl. Instrum. Meth. A* **2005**, *551*, 88.
(27) Soper, A. K. Rutherford Appleton Laboratory Technical Report RAL-TR-2011-013, 2011; Soper, A. K.; Buchanan, P. *Personal Communication*, 2004.
(28) Hannon, A. C.; Howells, W. S.; Soper, A. K. *IOP Conf. Ser.* **1990**, *107*, 193.
(29) Wright, A. C. *Adv. Struct. Res. Diffr. Methods* **1974**, *5*, 1.
(30) Lorch, E. *J. Phys. C* **1969**, *2*, 229.
(31) Larson, A. C.; Dreele, R. B. V. Los Alamos National Laboratory Report LAUR 86-748, 1994; Toby, B. H. *J. Appl. Crystallogr.* **2001**, *34*, 210.
(32) Farrow, C. L.; Juhas, P.; Liu, J. W.; Bryndin, D.; Bozin, E. S.; Bloch, J.; Proffen, T.; Billinge, S. J. L. *J. Phys.: Condens. Matter* **2007**, *19*, 335219.
(33) Subramanian, M. A.; Aravamudan, G.; Rao, G. V. S. *Prog. Solid State Chem.* **1983**, *15*, 55.
(34) Shannon, R. D. *Acta Cryst. A* **1976**, *32*, 751.
(35) Andersson, S.; Wadsley, A. D. *Acta Crystallogr.Sect. C; Cryst. Struct. Commun.* **1962**, *15*, 194.
(36) Sears, V. F. *Neutron News* **1992**, *3*, 26.
(37) Sasaki, T.; Ukyo, Y.; Kuroda, K.; Arai, S.; Muto, S.; Saka, H. *J. Ceram. Soc. Jpn.* **2004**, *112*, 440.
(38) Beyerlein, R. A.; Horowitz, H. S.; Longo, J. M.; Leonowicz, M. E.; Jorgensen, J. D.; Rotella, F. J. *J. Solid State Chem.* **1984**, *51*, 253.
(39) Ismunandar.; Kennedy, B. J.; Hunter, B. A.; Vogt, T. *J. Solid State Chem.* **1997**, *131*, 317.
(40) Brese, N. E.; O'Keefe, M. *Acta Crystallogr., Sect. B* **1991**, *47*, 192.
(41) Vanderah, T. A.; Levin, I.; Lufaso, M. W. *Eur. J. Inorg. Chem.* **2005**, 2895.
(42) Blundred, G. D.; Bridges, C. A.; Rosseinsky, M. J. *Angew. Chem., Int. Ed.* **2004**, *43*, 3562.
(43) Bastow, T. J.; Gibson, M. A.; Forwood, C. T. *Solid State Nucl. Magn. Reson.* **1998**, *12*, 201. Bastow, T. J. *Chem. Mater.* **1999**, *11*, 3518.
(44) Harunsani, M. H.; Oropeza, F. E.; Palgrave, R. G.; Egdell, R. G. *Chem. Mater.* **2010**, *22*, 1551.
(45) Grey, C. P.; Dobson, C. M.; Cheetham, A. K.; Jakeman, R. J. B. *J. Am. Chem. Soc.* **1989**, *111*, 505.
(46) Tunstall, D. P.; Patou, S.; Liu, R. S.; Kao, Y. H. *Mater. Res. Bull.* **1999**, *34*, 1513.
(47) Mitchell, M. R.; Reader, S. W.; Johnston, K. E.; Pickard, C. J.; Whittle, K. R.; Ashbrook, S. E. *Phys. Chem. Chem. Phys.* **2011**, *13*, 488.
(48) Fally, F.; Perrichon, V.; Vidal, H.; Kaspar, J.; Blanco, G.; Pintado, J. M.; Bernal, S.; Colon, G.; Daturi, M.; Lavalley, J. C. *Catal. Today* **2000**, *59*, 373. Fornasiero, P.; Montini, T.; Graziani, M.; Kaspar, J.; Hungria, A. B.; Martinez-Arias, A.; Conesa, J. C. *Phys. Chem. Chem. Phys.* **2002**, *4*, 149.
(49) Laachir, A.; Perrichon, V.; Badri, A.; Lamotte, J.; Catherine, E.; Lavalley, J. C.; Elfallah, J.; Hilaire, L.; Lenormand, F.; Quemere, E.; Sauvion, G. N.; Touret, O. *J. Chem. Soc., Faraday Trans.* **1991**, *87*, 1601.
(50) Fu, Q.; Weber, A.; Flytzani-Stephanopoulos, M. *Catal. Lett.* **2001**, *77*, 87.
(51) Germani, G.; Schuurman, Y. *AIChE J.* **2006**, *52*, 1806.